Journal of Applied Physics

Cation distribution and magnetic properties of Zn-substituted $CoCr_2O_4$ nanoparticles

Cite as: J. Appl. Phys. **123**, 223905 (2018); https://doi.org/10.1063/1.5027137
Submitted: 28 February 2018 . Accepted: 30 May 2018 . Published Online: 14 June 2018

G. Jagadish Kumar, Alok Banerjee, A. S. K. Sinha, Y. Su, K. Nemkovski, and Chandana Rath

Cation distribution and magnetic properties of Zn-substituted $CoCr_2O_4$ nanoparticles

G. Jagadish Kumar,[1] Alok Banerjee,[2] A. S. K. Sinha,[3] Y. Su,[4] K. Nemkovski,[4] and Chandana Rath[1,a)]

[1]*School of Materials Science and Technology, Indian Institute of Technology (BHU), Varanasi 221005, India*
[2]*UGC-DAE Consortium for Scientific Research, University Campus, Khandwa Road, Indore 452001, India*
[3]*Chemical Engineering and Technology, Indian Institute of Technology (BHU), Varanasi 221005, India*
[4]*Forschungszentrum Jülich GmbH, Jülich Centre for Neutron Science (JCNS) at Heinz Maier-Leibnitz Zentrum (MLZ), Lichtenbergstr. 1, 85748 Garching, Germany*

(Received 28 February 2018; accepted 30 May 2018; published online 14 June 2018)

$CoCr_2O_4$ is a normal spinel where Co occupies the tetrahedral (A) site and Cr occupies the octahedral (B) site; it is important to examine the cation distribution and magnetic properties by substituting a non-magnetic ion like Zn. In this context, we have synthesized pure phase $Zn_xCo_{1-x}Cr_2O_4$ ($x = 0.05, 0.1$) of crystallite size 10 nm through conventional co-precipitation technique. Fourier transform of Co, Zn, and Cr K-edge spectra obtained from extended X-ray absorption fine structure demonstrates that while Co and Zn prefer the A site, Cr strongly occupies the B site. The paramagnetic to long range ferrimagnetic transition, T_C, decreases from 97 K in $CoCr_2O_4$ (bulk) to 87.4 K at $x = 0.1$ with an intermediate T_C of 90 K at $x = 0.05$. The decrease in T_C is ascribed to decrease in A-B exchange interaction confirming the preferential occupation of Zn^{2+} ions towards the A site. The spin-spiral transition, T_S, decreases from 27 K in bulk ($CoCr_2O_4$) to 24 K at $x = 0.1$ followed by a spin lock-in transition, T_L, observed at 10 K which remains unchanged with increase in Zn concentration. The diffuse neutron scattering in both compositions shows the evidence of long range spiral ordering in contrast to the simultaneous formation of long and short range order in single crystals of $CoCr_2O_4$. The decrease in maximum magnetization from 9 to 8 emu/g and an increase in coercivity from 3.2 to 5.2 kOe at 2 K with an increasing Zn concentration from 0.05 to 0.1 have been explained by considering the Yafet-Kittel model. *Published by AIP Publishing*. https://doi.org/10.1063/1.5027137

I. INTRODUCTION

Transition metal oxides with the spinel structure are important magnetic materials having the general formula of AB_2O_4, where A and B represent tetrahedral and octahedral sites, respectively, coordinated by oxygen atoms. While in a normal spinel, the divalent cations occupy the A site and trivalent cations prefer the B sites, in an inverse spinel, the divalent cations prefer one of the B sites and the trivalent cations are equally distributed among A and B sites. In mixed spinels, however, two or more different kinds of divalent cations are distributed between A and B sites.[1] Thus, the magnetic behavior in these compounds is sensitive to the type of cations and their distribution among A and B sites of the spinel lattice. As a result, properties can be modulated and materials can be tuned for technological applications. $CoCr_2O_4$, one of the normal spinels, where Co^{2+} ions occupy the A site and Cr^{3+} ions occupy the B sites, is unique as it not only displays uniform polarization and spatially modulated magnetism but also exhibits uniform magnetization in the conical cycloid state. Yamasaki *et al.*[2] discovered the multiferroicity in the $CoCr_2O_4$ single crystal by demonstrating the magnetically driven reversal of electric polarization. Bulk and nanoparticles of $CoCr_2O_4$ show paramagnetic to long range ferrimagnetic transition, T_C, at 94–97 K and ferrimagnetic to a conical spin-spiral transition, T_S, at 23–31 K.[3,4] Besides T_C and T_S, we have shown an intermediate super-paramagnetic phase between 50 and 60 K in nanoparticles of $CoCr_2O_4$.[5] While spin-spiral transition is found to be incommensurate in a single crystal, we have shown a short range, commensurate spiral ordering in 50 nm particles, which is found to be absent in 10 nm particles.[4] Further decreasing the temperature below T_S, in a single crystal, Yamasaki *et al.*[2] show that the incommensurate conical spin-spiral order stabilizes down to the spin lock-in transition (T_L) which occurs at 15 K. We have demonstrated spin lock-in transition in 10 and 50 nm particles at 5 and 8.5 K, respectively, through the diffused neutron scattering experiment using polarized neutron.[4] In a single crystal of $CoCr_2O_4$, Tomiyasu *et al.*[3] have shown the simultaneous formation of a long-range ferrimagnetic component and develops an incommensurate short-range spiral order below 50 K. Severance *et al.*[6] have shown that the short-range magnetic order vanishes at 50 K as the intensity of the diffused magnetic peak diminishes to the background level. Using DFT+U method, Das *et al.*[7] have predicted the non-collinear spin structure of $CoCr_2O_4$ which is due to the comparable A-B and B-B exchange interactions. Spin-spiral and spin lock-in transitions are also evidenced from a large enhancement in spin-Hall magnetoresistance and spin-Seebeck effect in thin films of $CoCr_2O_4$.[8] The above exciting findings thus demand to be discussed after mixing A or B sites by

a)Author to whom correspondence should be addressed: crath.mst@iitbhu.ac.in

magnetic or non-magnetic ions when the size of the particles is reduced to the nanometer range. In this context, Kumar *et al.*[9] have observed an enhancement in T_C up to 200 K and spiral ordering temperature up to 40 K by increasing the Fe concentration up to 50%. Kemei *et al.*[10] have studied magnetic transitions in the normal spinel, $Mg_{1-x}Cu_xCr_2O_4$, and have reported that the Neel temperature (T_N) observed at 12.5 K at $x = 0$ increases to 128 K at $x = 1$. Kemei *et al.*[11] have reported the changes in structural ground states of $ZnCr_2O_4$ when 10% and 20% Co^{2+} cations are substituted on the nonmagnetic, Zn^{2+} site. It has been shown that when Co^{2+} ions are greater than or equal to 10%, the structural distortions that accompany antiferromagnetic ordering in $ZnCr_2O_4$ is suppressed. A rich sequence of magnetic transitions, such as T_C, T_S, and T_L, reported in few chromites, have not been studied in Zn substituted $CoCr_2O_4$ so far.

In this report, we have studied the structural and microstructural evolution in $Zn_xCo_{1-x}Cr_2O_4$ ($x = 0.05$, 0.1) nanoparticles, synthesized by the co-precipitation technique through X-ray Photoelectron Spectroscopy (XPS), X-ray diffraction (XRD), and Extended X-ray Absorption Fine Structure (EXAFS) techniques. While XPS shows the **valencies** of Co, Zn, and Cr as +2, +2, and +3, respectively, the pure cubic phase of $Zn_xCo_{1-x}Cr_2O_4$ is confirmed from XRD. EXAFS provides the evidence of distribution of Co^{2+}, Zn^{2+} towards A, and Cr^{3+} towards the B site. Magnetic transitions in $Zn_xCo_{1-x}Cr_2O_4$ ($x = 0.05$, 0.1) are examined from temperature dependent magnetization, ac susceptibility, and neutron scattering using polarized neutron. Temperature dependent ac susceptibility confirms the coexistence of spin glass (SG) and cluster glass in $x = 0.05$ which is absent in $x = 0.1$.

II. EXPERIMENTAL DETAILS

A. Synthesis method

Fine particles of $Zn_xCo_{1-x}Cr_2O_4$ with $x = 0.05$ and 0.1 were prepared by the wet chemical co-precipitation technique. Stoichiometric amount of zinc nitrate [$Zn(No_3)_2{\cdot}6H_2O$] with 99.5% purity, cobalt nitrate [$Co(No_3)_2{\cdot}6H_2O$] of 99% purity, and chromium nitrate [$Cr(No_3)_3{\cdot}9H_2O$] of 98% purity purchased from Himedia Laboratories, India were mixed together and kept at 70 °C under stirring. 1 M NaOH solution was added to the mixed solution under continuous stirring till complete precipitation takes place. The precipitate was filtered several times and was washed with distilled water followed by acetone. The powder was dried at 120 °C and finally was calcined at 500 °C for 5 h.

B. Characterizations

The calcined powders were characterized through X-ray diffraction using an 18 kW rotating anode (Cu Ka) based Rigaku powder diffractometer, operating in the Bragg-Brentano geometry and was fitted with a graphite monochromator in the diffracted beam. Transmission electron microscope (TEM, Technai) was used to study the morphology and size distribution of particles. For TEM measurement, 1 mg of powder sample was mixed with 10 ml of ethanol followed by dispersion using a sonicator for 90 min and a probe sonicator for 5 min. A drop of the well dispersed solution was placed over the carbon coated copper grid, and the grid was dried at room temperature for 12 h. X-ray photoelectron spectra were collected in order to determine the valency of the elements like Co, Cr, and Zn. EXAFS spectroscopy has revealed itself as a powerful technique for the structural characterization of the local atomic environment of individual atomic species, including bond distances, coordination numbers, and type of nearest neighbors surrounding the central atom. EXAFS measurements were carried out at the Energy scanning EXAFS beam line (BL-9) in transmission mode at the INDUS-2 Synchrotron Source (2.5 GeV, 100 mA) at the Raja Ramanna Centre for Advanced Technology (RRCAT), Indore, India.[12,13] $Zn_xCo_{1-x}Cr_2O_4$ ($x = 0.05$, 0.1) samples of an appropriate weight have been mixed thoroughly with cellulose powder to obtain a total weight of 100 mg. Hydraulic press was used to prepare pellets of 15 mm diameter. EXAFS data analysis programs available within the IFEFFIT software package were used for analysis.[14] ATHENA software is used for EXAFS data processing including conversion of raw data to μ(E) spectra, background subtraction, Fourier transforming, and plotting. ARTEMIS software was used to fit the experimental data with the theoretical spectra. We carried out polarized neutron scattering measurement using Diffuse Neutron Scattering (DNS) spectrometer, at FRM II, which was operated by Jülich Centre for Neutron Science at Garching, Germany. The sample environment is a top loading closed cycle refrigerator in which sample is mounted on a cylindrical aluminum holder. The wavelength of monochromator is 4.2 Å. The monochromator is horizontally and vertically adjustable one having double focusing. XYZ-polarization analysis allowed the magnetic scattering to be separated from the nuclear-coherent and spin-incoherent contributions. The magnetic properties of the samples were measured by Magnetic Properties Measurement System (MPMS) of Quantum Design, Inc. AC susceptibility measurements were done at 3, 31, 231, and 966 Hz by applying a dc field of 3 Oe.

III. RESULTS AND DISCUSSION

X-ray Photoelectron Spectroscopy (XPS) technique is used to investigate the valency of transition metals in $Zn_xCo_{1-x}Cr_2O_4$ ($x = 0.05$, 0.1). Figure 1 shows the characteristic core-level spectra of Co 2p and Cr 2p of $Zn_xCo_{1-x}Cr_2O_4$ ($x = 0.05$, 0.1) fitted with two Gaussian peaks using XPSpeak 4.1 software with Shirley background.

The two strong peaks observed at 782.8 eV and 798.3 eV, shown in Fig. 1(a), correspond to Co $2p_{3/2}$ and Co $2p_{1/2}$, respectively. The binding energy difference between $2p_{1/2}$ and $2p_{3/2}$ sublevels of Co 2p is found to be 15.5 eV and 15.4 eV for $x = 0.05$ and 0.1, respectively. The observed difference in binding energy between two sublevels of Co confirms the +2 oxidation state of Co.[15] The satellite peaks observed at higher binding energy compared to their core peak could be due to the shake up process of the Co 2p level. The obtained binding energy difference between $2p_{1/2}$ and $2p_{3/2}$ sublevels of chromium, shown in Fig. 1(b), is 9.6 eV

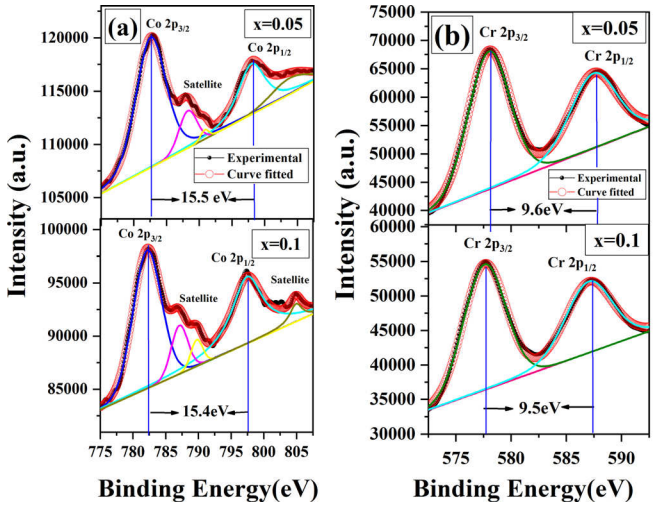

FIG. 1. X-ray photoelectron spectroscopy of (a) Co and (b) Cr elements for $Zn_xCo_{1-x}Cr_2O_4$, x = 0.05 and 0.1.

and 9.5 eV for x = 0.05 and 0.1, respectively, which confirms the +3 oxidation state of chromium.[15]

Figure 2 depicts the X-ray diffraction patterns of $Zn_xCo_{1-x}Cr_2O_4$ (x = 0.05, 0.1). The prominent Bragg peaks at 30.45°, 35.75°, 43.5°, 54°, 57.5°, and 63.1° correspond to (220), (311), (400), (422), (511), and (440) of the cubic phase of $CoCr_2O_4$ (JCPCS file No. 780711), respectively. No characteristic reflection peaks derived from other contaminants such as $CoCr_2O_4$, cobalt, or chromium oxides are detected, which eliminate the presence of impurities within the detection limit of the XRD instrument. All XRD patterns are fitted well with the $Fd\bar{3}m$ space group using the Le-bail profile fitting of Fullprof program. In Fig. 2, a solid line with square represents observed pattern, sphere represents calculated data after fitting, and the difference between the observed and calculated data is shown in the bottom line. The Bragg peaks are represented by the tick marks above the difference plot. The lattice parameter (a) obtained from the Le-Bail profile refinement decreases from 8.32 Å to 8.31 Å with increase in Zn concentration from 5 to 10 mol. %. Although the ionic radius of Zn^{2+} is 0.74 Å, which is slightly higher than that of Co^{2+} ion (0.72 Å), we have observed a small contraction instead of expansion in unit cell volume with increase in Zn concentration. Similar decrease in unit cell volume is also observed by Melot *et al.*[16] in bulk $Co_xZn_{1-x}Cr_2O_4$. The possible reason behind the contraction of unit cell volume could be due to the less ionic nature of Zn than Co, and/or due to decrease in A-B repulsion. The crystallite size of $Zn_xCo_{1-x}Cr_2O_4$ (x = 0.05, 0.1) samples is estimated using the Debye-Scherrer formula shown in the following equation, after correcting the instrumental broadening:

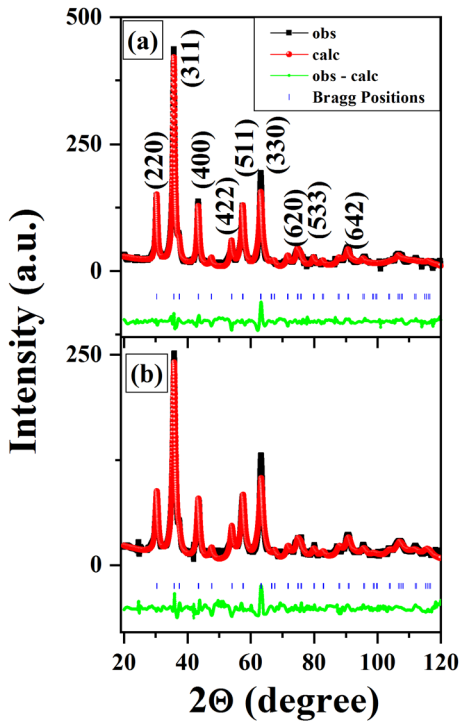

FIG. 2. X-ray diffraction (XRD) patterns of $Zn_xCo_{1-x}Cr_2O_4$ for (a) x = 0.05 and (b) x = 0.1, fitted with the space group $Fd\bar{3}m$ using the Le-Bail profile refinement.

$$D_{XRD} = \frac{0.89\,\lambda}{\beta \cos\theta}. \quad (1)$$

D_{XRD} is the crystallite size, λ is the wavelength of X-ray, β is the full width at half-maximum (FWHM), and Θ is the Bragg angle. The mean crystallite size is found to be ~10 nm for both x = 0.05 and 0.1 samples.

Figures 3(a) and 4(a) depict the transmission electron micrographs for x = 0.05 and 0.1, respectively. The micrographs show well distributed particles of cuboid shape. From the particle size histogram shown in Figs. 3(b) and 4(b), the average particle size is found to be ~10 and ~8 nm for x = 0.05 and 0.1, respectively, which match well with the crystallite size estimated from Scherrer's equation. The distinguished diffraction rings observed from the selected area electron diffraction (SAED) pattern, is depicted in Figs. 3(c) and 4(c), indexed as (220), (311), (400), (440), and (511) of Fd-3m. Figures 3(d) and 4(d) depict the high resolution TEM images of well-defined atomic planes. The interplanar spacing of ~0.29 nm and ~0.26 nm corresponds to (220) and (311) of Fd-3m, cubic structure in both samples. Although crystallite size does not change with Zn concentration, we have studied the cation distribution using EXAFS in x = 0.05 and 0.1 which is essential to define as Zn strongly prefers the A-site.

EXAFS analysis for Co, Zn, and Cr K-edges has been carried out using Athena and Artemis program coupled with the FEFF 8.0 code for $Zn_xCo_{1-x}Cr_2O_4$ (x = 0.05, 0.1).

Figure 5 depicts the normalized absorption versus energy for Co K-edge. Comparing the maximum absorption peak (K-edge) in the EXAFS spectra of Co, Cr, and Zn with standard samples of CoO, YCr_2O_3, and ZnO, it is confirmed that valencies of Zn, Co and Cr are +2, +2 and +3, respectively. In addition, we observed that the energy of K-edge peak does not change with increase in Zn concentration. While the main peak in Co spectra is associated with a small pre-edge peak (inset of Fig. 5), the same is absent in both Cr and Zn K-edges. While the main peak observed in Co spectra

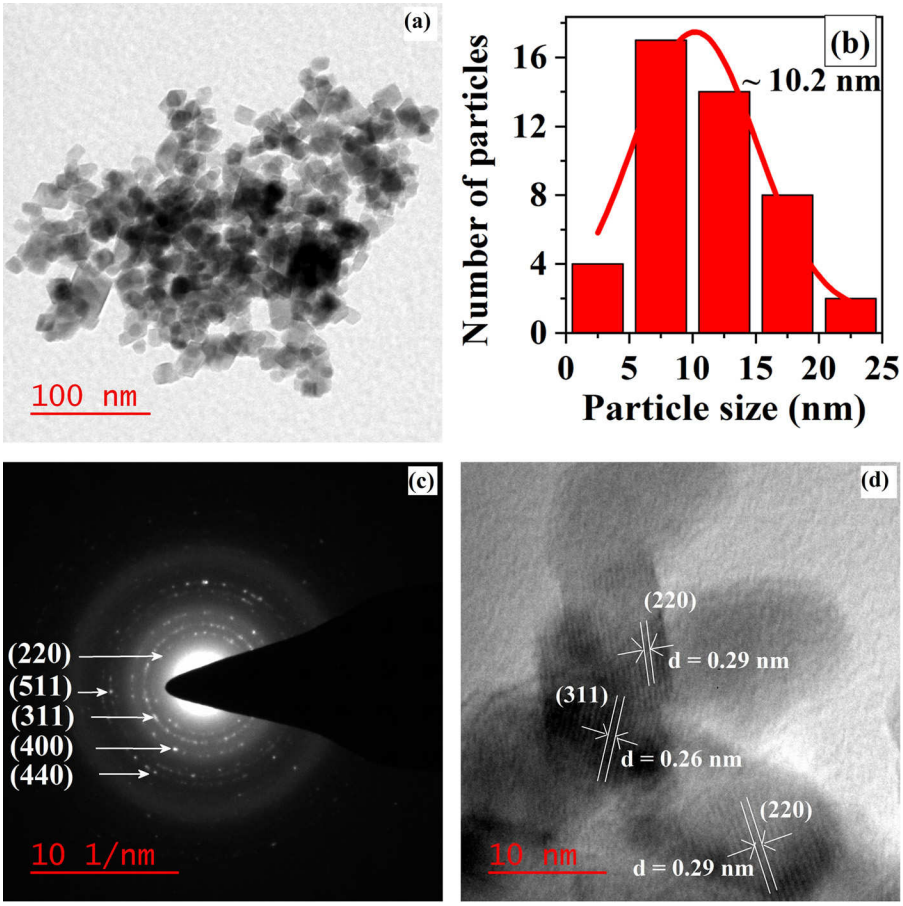

FIG. 3. (a) Transmission electron micrograph of $Zn_{0.05}Co_{0.95}Cr_2O_4$, (b) particle size histogram, (c) Selective Area Electron Diffraction (SAED) pattern, and (d) high resolution TEM image.

is attributed to 1s to 4p transition, the pre-edge peak is due to 1s to 3d quadrapole and from 1s to 3d/4p (hybridized orbitals) dipole transitions.[17,18] The intensity of quadrupole transition is in general very low and the degree of hybridization of the transition metal 3d states with 4p states affects the pre-edge peak intensity which in turn is affected by the degree of centrosymmetry of the photon absorber. The mixing of the 4p and 3d orbitals is forbidden in the octahedral site due to the presence of inversion symmetry, and it is allowed in the tetrahedral symmetry.[17,18] Absence of the pre-edge peak in the Cr K-edge confirms that Cr occupies the B site. However, absence of the pre-edge peak in Zn is due to completely filled 3d states of Zn.[19] The pre-edge peak intensity of Co increases with the increase in Zn concentration which indicates that Co prefers tetrahedral symmetry. Further, the qualitative information about the local structure around Zn, Co, and Cr atoms could be obtained from the Fourier transform of the respective K-edge spectra.

Figure 6 depicts the Fourier transform in R-space for Zn, Co, and Cr, respectively. In ferrites, the radial distance of the first coordinate shell is considered to differentiate the site distribution of cations at the A and B sites. $CoCr_2O_4$ crystallizes in the normal spinel structure with Co preferring A site and Cr occupying the B site. The radial distribution of the first coordination shell in Co and Cr environments is found to be 1.6 Å in $CoCr_2O_4$.[4] The position of second peak (i.e., the distance of second coordination shell) observed at different radial distances is considered to determine the distribution of cations in two different environments. Similarly in the present case, we also observed the first coordination shell to be nearly same (~1.6 Å) in Zn, Co, and Cr which eliminates the possibility of finding the distribution of the cations in A and B sites. Therefore, the position of the second coordination shell is taken into consideration to determine the distribution of cations. In the case of Zn and Co, the position of second peak is observed at r ~ 3 Å which indicates that Zn and Co prefer to occupy the A site. In the case of Cr, the position of second peak is observed at r ~ 2.45 Å which indicates that Cr prefers to occupy the B site. After obtaining the qualitative idea of the local structure around Zn, Co, and Cr, we have fitted the reduced EXAFS data in R-space. The raw FT-EXAFS spectra, background corrected and energy calibrated spectra, are fitted using IFEFFIT (ARTEMIS) software for Zn, Co, and Cr in x = 0.05 and 0.1 in order to obtain the bond distance (r) and mean-square disorder parameter (σ^2). It is well known that σ^2, the amplitude function, is the mean-square displacement of the path-length due to the thermal or static disorder and is strongly correlated with the number of nearest neighbors. Lattice parameters and atomic coordinates are used as inputs to generate an FEFF input file, with Cr, Zn, and/or Co as the core for the corresponding Cr, Zn, and/or Co K-edge spectra. As Zn replaces Co at the A-site, we have used the atomic coordinates of Co to fit the Zn K-edge.

The photoelectron scattering paths are then calculated and the experimental data are fitted up to 4 Å in the R-space, and the results are as shown in Fig. 7. From Table I, we notice that the bond length (r) observed between the central

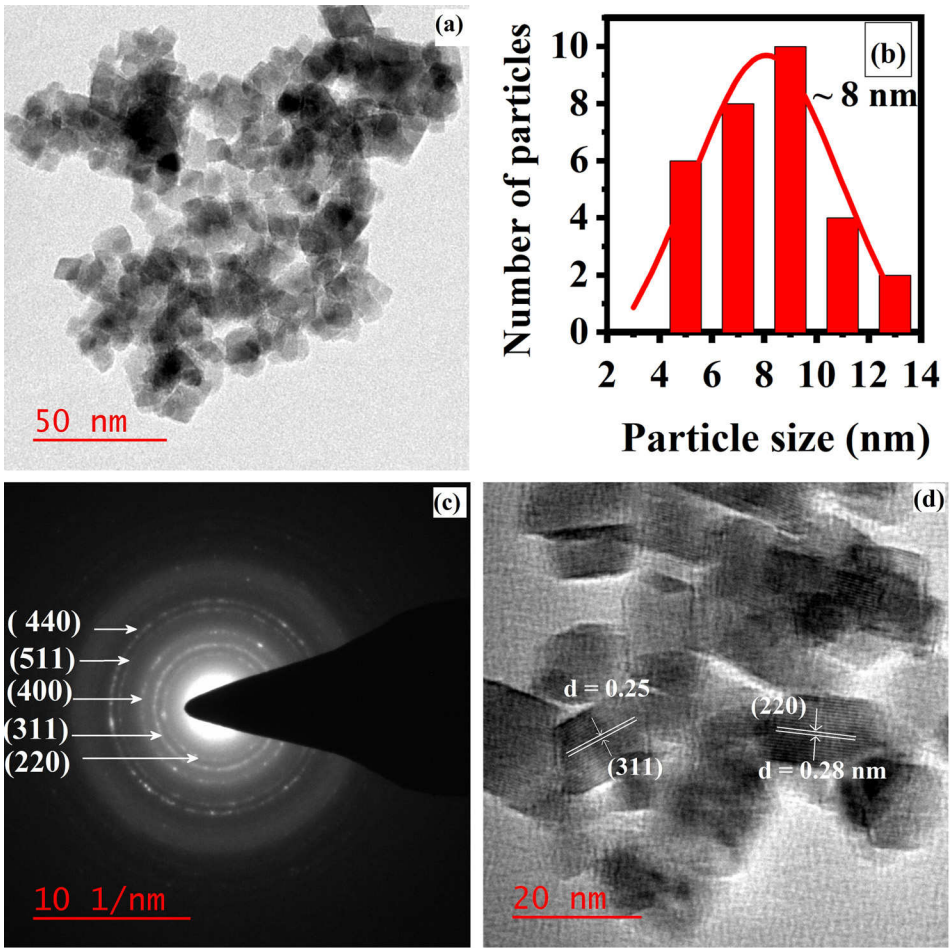

FIG. 4. (a) Transmission electron micrograph of $Zn_{0.1}Co_{0.9}Cr_2O_4$, (b) particle size histogram, (c) Selective Area Electron Diffraction (SAED) pattern, and (d) high resolution TEM image.

atom and second coordination shell of Co, Zn, and Cr is 3.48, 3.46, and 2.91 Å for x = 0.05. It is observed that there is no significant change in bond length with increase in Zn concentration. Hence, we conclude that Co and Zn ions occupy the A site and Cr strongly prefers the B site. The results corroborate with our previous report on $CoCr_2O_4$ where we have shown that Co atoms are tetrahedrally coordinated by 12 Cr ions at 3.45 Å as second nearest neighbors and Cr atoms are octahedrally coordinated by 6 Cr ions at 2.96 Å as the second nearest neighbours.[21] While the cation distribution does not change by incorporating Zn in $CoCr_2O_4$, we further examine the effect on magnetic properties by analyzing the temperature and external magnetic field dependent magnetization in $Zn_xCo_{1-x}Cr_2O_4$ (x = 0.05, 0.1).

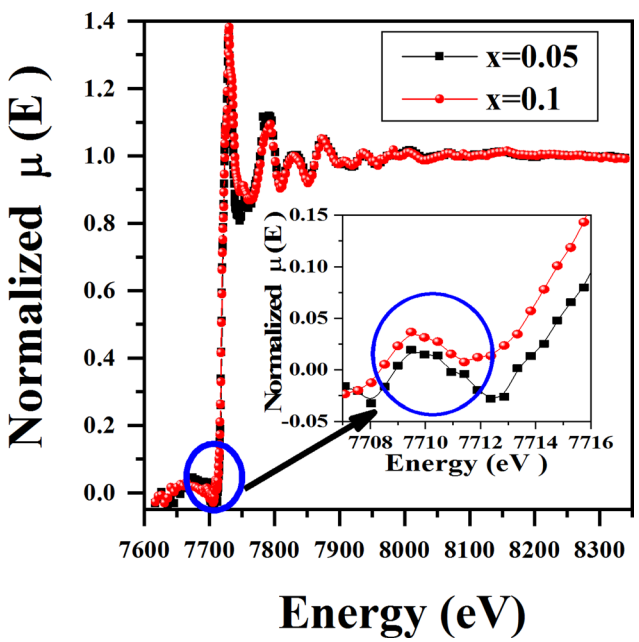

FIG. 5. Comparison of the EXAFS spectra of Co K-edge for $Zn_xCo_{1-x}Cr_2O_4$ (x = 0.05, 0.1) nanoparticles. The inset of Fig. 5 shows the expanded view of the pre-edge peak.

Figure 8 depicts the temperature dependence of zero-field-cooled (ZFC) and field-cooled (FC) dc susceptibility with an applied field of 500 Oe. With the decrease in temperature from 300 K, around 80 K, both M_{FC} and M_{ZFC} show a rapid increase, which is indicative of paramagnetic to long-range ferrimagnetic transition, i.e., T_C. It is derived by extrapolating the linear part of magnetization to zero in the high temperature regime. T_C is found to be 90 K and 87.4 K for x = 0.05 and 0.1, respectively, which is lower than that of T_C of bulk and polycrystalline $CoCr_2O_4$ (95 K and 97 K).[2,20,21] As T_C is decided by A-B exchange interaction in spinels, decrease in T_C with increase in Zn concentration thus confirms that A-B exchange interaction decreases due to replacement of Co^{2+} by non-magnetic, Zn^{2+} at the A site. With decrease in temperature, both M_{ZFC} and M_{FC} show a large increase and reaches to a maximum at temperature T_{max}, followed by a splitting at a temperature called irreversible temperature, T_{irr}. T_{max} and T_{irr} are observed at 56 K and

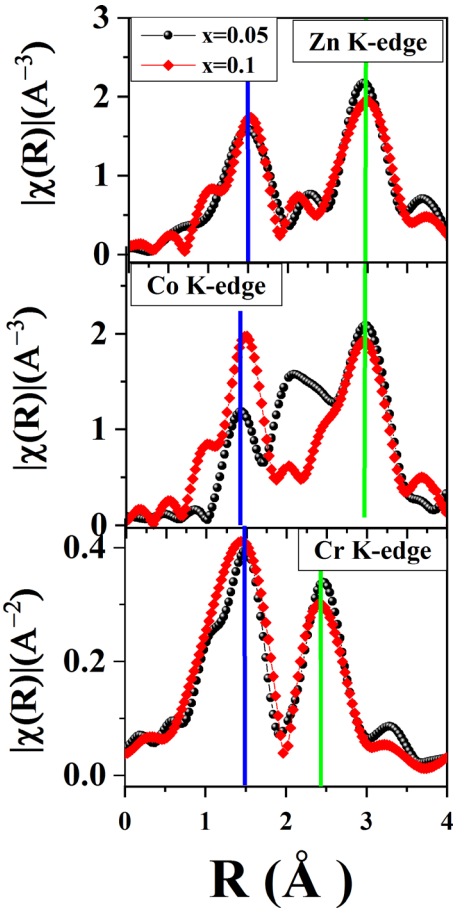

FIG. 6. Fourier transforms moduli of the χ(R) EXAFS signals for Zn, Co, and Cr K-edges data.

66 K, respectively, in x = 0.05, which shift to 66 K and 73 K, respectively, with increase in Zn concentration to 10 mol. %. Higher values of T_{irr} than T_{max} in both samples indicate the presence of large spin clusters which are ordered at higher temperature. T_{max} generally indicates either the blocking temperature (T_B) of superparamagnets (SPM) or the spin-freezing temperature (T_f) of spin glasses, which could be further confirmed from ac susceptibility measurement. dχ/dT depicted in Figs. 8(c) and 8(d) shows, in addition to T_C at 90 K and 87.4 K, an anomaly at 26 K and 24 K which is the spiral-spiral transition, T_S, for x = 0.05 and 0.1, respectively. In bulk and single crystals of $CoCr_2O_4$, while T_S is observed at 31 K (Ref. 21) and 24 K (Ref. 3) in the case of nanoparticles of $CoCr_2O_4$, we have shown T_S at ∼25 ± 1 K which remains unaffected by varying the size from 10 to 50 nm.[4] Another magnetic anomaly corresponds to spin lock-in transition (T_L) observed at 15 K in a single crystal of $CoCr_2O_4$ which is found to be absent after incorporating Zn^{2+} in the present case.[3] However, we have shown in our previous work on $CoCr_2O_4$ that T_L increases from 5 K to 8.5 K with increase in size from 10 to 50 nm.[4] The spin-spiral transition (T_S) and spin lock-in transition (T_L) temperatures are further probed through Diffused Neutron Scattering (DNS) using the polarized neutron source available at FRM II, Germany. Along three orthogonal directions, the sequence of magnetic transitions such as T_C, T_S, and T_L, which are observed in $CoCr_2O_4$, are analyzed in the present work.

The typical magnetic, nuclear, and spin-incoherent scattering in $Zn_xCo_{1-x}Cr_2O_4$ (x = 0.05, 0.1) particles is depicted in Figs. 9(a) and 9(b), respectively. Magnetic Bragg peaks such as (111) and (220) have been measured in detail by spin flip scattering in the range of 3.5 K to 100 K. With decrease in temperature from 100 K, the reflection of (111) peak is getting broad and asymmetric in both x = 0.05 and 0.1 (figure not shown here). The fundamental reflections are coherent Bragg reflections up to 100 K and above that the intensity of the (111) reflection diminishes to the background level. It indicates that the ferrimagnetic component exhibits a long-range order below 100 K and 90 K for x = 0.05 and 0.1, respectively. Due to broad and asymmetric nature of (111) peak, we have de-convoluted it into two peaks in order to calculate the intensity of fundamental reflection as well as the satellite reflection.

The intensity of the fundamental reflection (111) decreases with increase in Zn concentration in both x = 0.05 and 0.1 as shown in Fig. 10. The intensity of (111) peak changes its slope at ∼26 K and ∼24 K for x = 0.05 and 0.1, respectively, which indicates spin-spiral transition, T_S. The variation in intensity at T_S is the evidence of the tilting of the magnetic moment. Though the intensity of the satellite peak is found to be weak in x = 0.1, it is observed that the intensity increases slowly with decrease in temperature in both samples. The intensity is getting flat at 10 K with decrease in

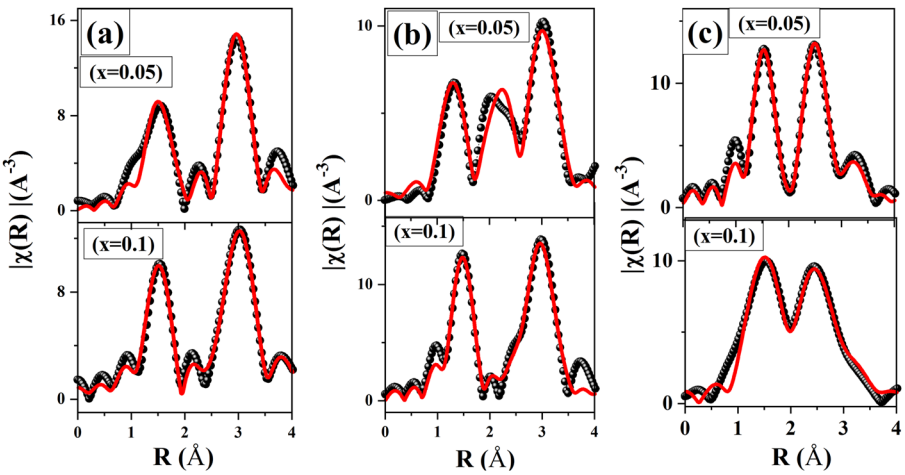

FIG. 7. (a) Zn K-edge, (b) Co K-edge, and (c) Cr K-edge Fourier transform EXAFS data with real (r) parts of the phase plotted with fitted curves for $Zn_xCo_{1-x}Cr_2O_4$ (x = 0.05, 0.1).

TABLE I. Fitting parameters like bond length and disorder factors deduced from EXAFS fitting (a) Zn K-edge, (b) Co K-edge, and (c) Cr K-edge, respectively.

(a) Zn edge			
Path	Parameter	x = 0.05	x = 0.1
Zn-O	r/Å	1.95	1.94
	σ^2	0.009	0.002
Zn-Cr	r/Å	3.46	3.46
	σ^2	0.0013	0.0055
Zn-O	r/Å	3.41	3.2
	σ^2	0.0017	0.0064
Zn-Zn	r/Å	3.626	3.62
	σ^2	0.0023	0.0045
(b) Co edge			
Path	Parameter	x = 0.05	x = 0.1
Co-Cr	r/Å	1.96	1.94
	σ^2	0.0026	0.0031
Co-Cr	r/Å	3.48	3.42
	σ^2	0.0039	0.0089
Co-O	r/Å	3.40	3.27
	σ^2	0.0083	0.0437
Co-Co	r/Å	2.63	2.19
	σ^2	0.0068	0.0235
(c) Cr edge			
Path	Parameter	x = 0.05	x = 0.1
Cr-O	r/Å	1.964	1.965
	σ^2	0.0026	0.0019
Cr-Cr	r/Å	2.91	2.96
	σ^2	0.0039	0.0028
Cr-Co	r/Å	3.407	3.339
	σ^2	0.0083	0.0147

temperature which is noted as spin lock-in transition, T_L. Although no spin lock-in transition is reported from neutron scattering experiments done by Tomiyasu *et al.*[3] in our previous work on $CoCr_2O_4$, as well as in the present case, we have demonstrated T_S and T_L from diffused neutron scattering. The atomic arrangement in both samples remains disordered even at very low temperature, resulting in a relatively flat diffusive background. As a consequence, we have observed a non-saturation behavior of magnetization by applying an external magnetic field of 140 kOe as discussed later. A similar diffuse background due to magnetic disorder has been proposed by Golosovsky *et al.*[22] The correlation length of the spiral order (ξ) is calculated by taking the inverse of the half width at half-maxima (HWHM). The half width at half-maxima of the satellite reflection is determined using Lorentzian distribution by the method of least squares in x = 0.05 and 0.1.

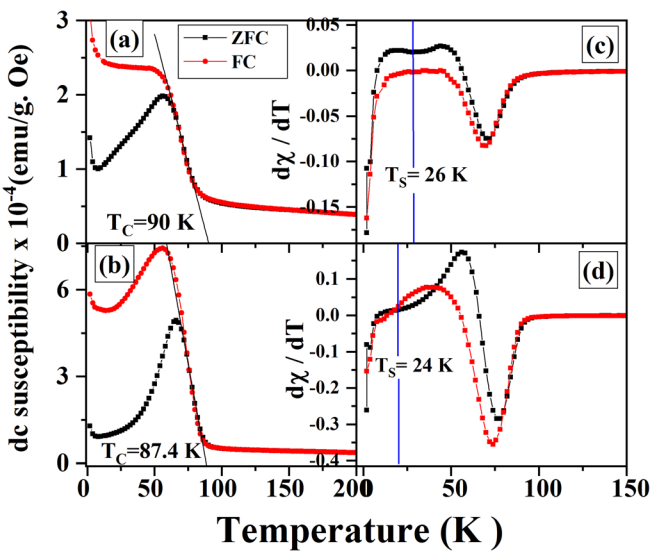

FIG. 8. DC susceptibility vs. temperature at 500 Oe for $Zn_xCo_{1-x}Cr_2O_4$, (a) x = 0.05 and (b) x = 0.1. (c) and (d) show dχ/dT of x = 0.05 and 0.1, respectively.

The temperature dependent correlation length for x = 0.05 and 0.1 is shown in Fig. 11. As temperature decreases, ξ increases slowly up to 30 K. Further, decrease in temperature down to 3.5 K leads to a sharp increase in the correlation length. The value of ξ at 3.5 K is more than 6 nm for x = 0.05 and 0.1, respectively, which are higher than 3.1 nm of a single crystal $CoCr_2O_4$.[3] Yamasaki *et al.*[2] investigated the low-temperature magnetic phase diagram of $CoCr_2O_4$ and have found that the compound undergoes a transition to a conical spin structure with an incommensurate propagation vector Q ~ (0.63, 0.63, 0) at T_N = 26 K, and spin lock-in transition, T_L, around 15 K.[2] Dwight and Menyuk[23] predicted that spiral ordering is incommensurate and the commensurate spiral order is observed due to some defects. The spiral order observed in our case is twice than that of $CoCr_2O_4$ and is diffused in nature unlike in $CoCr_2O_4$ nanoparticles.[22] We confirm that the long-range ferrimagnetic to paramagnetic transition as well as large spiral ordering after incorporation of Zn in $CoCr_2O_4$ in contrast to the short range spiral ordering is observed in $CoCr_2O_4$.[4]

In order to examine the magnetically ordered state in these nanoparticles, ac susceptibility measurements (χ' and χ'') with varying temperature and frequency have been undertaken and results are shown in Fig. 12.

The real (χ') and imaginary (χ'') parts of ac susceptibility at 3, 31, 231, and 966 Hz for x = 0.05 and 0.1 are shown in Figs. 12(a) and 12(b), respectively. The real part of ac susceptibility of x = 0.05 exhibits a broad peak at T_B with a shift towards higher temperature with increase in frequency, while it is found to be absent in x = 0.1. Figure 12(ii) clearly denotes the spin-spiral transition (T_S) at 26 K for x = 0.05 which is found to be absent in x = 0.1. For x = 0.05, the magnitude of χ' becomes smaller, and the low temperature tail of this peak decreases with increase in frequency. Such a frequency dependence of ac susceptibility is commonly observed in both spin glass and superparamagnetic systems. However, in our case, the shift in T_B with frequency is small (~0.1) which eliminates the possibility of the non-interacting superparamagnetic nature of the particles.[24] The frequency dependence of T_B explained using $\phi = \frac{\Delta T_B}{T_B \Delta \log_{10}(f)}$ gives the value of ϕ as 0.02. In general, the value of ϕ lies in between 0.005 and 0.08, ~0.03–0.06, and 0.3 for spin glass (SG), cluster spin glass (CG), and non-interacting superparamagnetic (SPM) particles, respectively.[25,26] The obtained value of 0.02 matches well with the SG rather than the non-interacting SPM particles. With increasing strength of interaction between the particles, one can encounter a collective

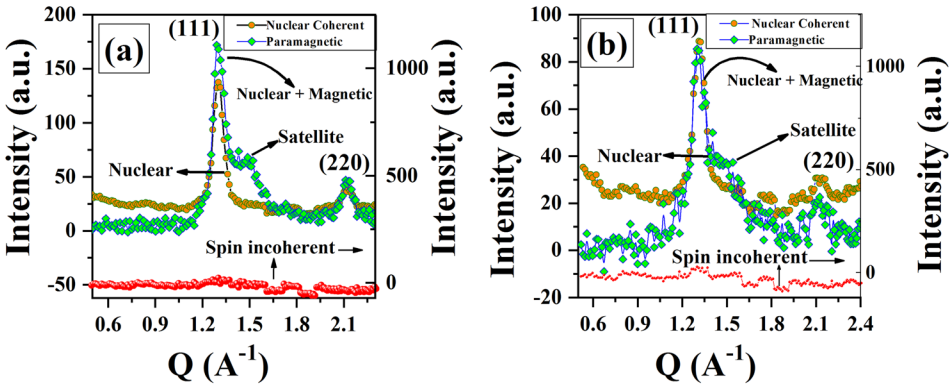

FIG. 9. Polarized neutron scattering data showing nuclear, magnetic, and spin-incoherent scattering for $Zn_xCo_{1-x}Cr_2O_4$, (a) x = 0.05, (b) x = 0.1, respectively.

behavior. In order to understand the inter-cluster interaction and its effect on the fluctuation dynamics, we have further analyzed Neel-Arrhenius, Vogel-Fulcher, and power law.[24] According to Neel-Arrhenius law, the relaxation time for an assembly of non-interacting superparamagnetic (SPM) particles is expressed as $\tau = \tau_0 \exp(E_a/K_BT)$, where E_a is the average anisotropy (activation) energy barrier equal to KV, K is the anisotropy constant, and V is the volume of the particle. τ_0 is a time constant that corresponds to the characteristic frequency.

The best fit is shown in Fig. 13(a). The value of τ_0 is found to be 3.5×10^{-51}, an unphysical value which eliminates the possibility of the non-interacting superparamagnetic nature of the particles. Further Vogel-Fulcher's law, $\tau = \tau_0 \exp\left[\frac{-E_a}{K_B(T_B - T_o)}\right]$, has been analyzed to explain the frequency dependent shift of T_B, where T_o is the Vogel-Fulcher temperature ($0 < T_o < T_B$) which represents strength of the inter-particle interaction and is varied in steps of 0.2 K in order to fit the data. τ_0 of 3.1×10^{-10} s, obtained from the best fit [Fig. 13(b)], is found to be three orders higher in magnitude than the spin-flip time of atomic magnetic moment ($\sim 10^{-13}$ s), which suggests the CG behaviour.[27] Further, the frequency dependent shift of the χ' fitted with power law

$$\tau = \tau_0 (T_f/T_g - 1)^{-z\nu}, \quad (2)$$

where τ_o is the microscopic flipping time of the fluctuating spins, T_g is the spin-glass transition temperature, z is the dynamical exponent, and ν is the usual critical exponent for the correlation length. The best fit of Eq. (2), shown in Fig. 13(c), gives the value of $z\nu$ as 9.9 which is of spin glass. The value of τ_0 obtained from the fit is 3×10^{-13} s which is also consistent with the spin glass behavior. The interaction effect in nanoparticles studied by Poddar *et al.*[28] shows that the strong dipolar interaction between nanoparticles would yield a spin-glass like behavior and the strength of interaction arises from the bulk crystalline and the surface anisotropy. The randomly induced spin disorder in x = 0.05 promotes the surface anisotropy and strengthens the dipolar interaction resulting in spin-glass nature. Hence for x = 0.05, the coexistence of both CG and SG behavior of particles is confirmed from Vogel-Fulcher law and power law. In the case of x = 0.1, the magnetic moment of a sub-lattice decreases with Zn which weakens the surface spin disorder in nanoparticles and hence results in weak dipolar interaction. Thus, we do not observe any dispersion of susceptibility with frequency in x = 0.1. The field dependent magnetization measurement is probed further in order to find out the relative alignments of the spins and their magnitude.

The magnetization is measured after applying magnetic field of 140 kOe in x = 0.05 and 0.1 at different temperatures such as 2, 20, and 50 K, i.e., below T_C. A typical variation in

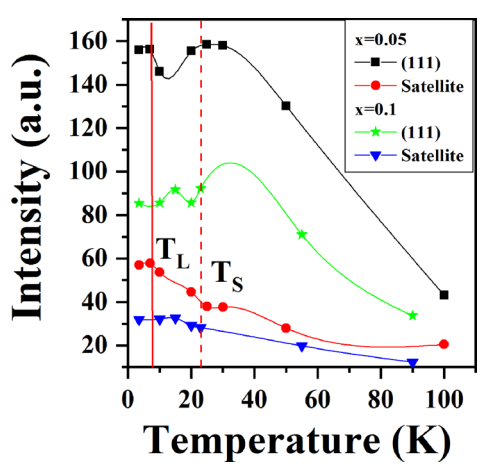

FIG. 10. Temperature dependence of integrated intensity of the fundamental magnetic (111) reflection and satellite reflection of x = 0.05 and x = 0.1.

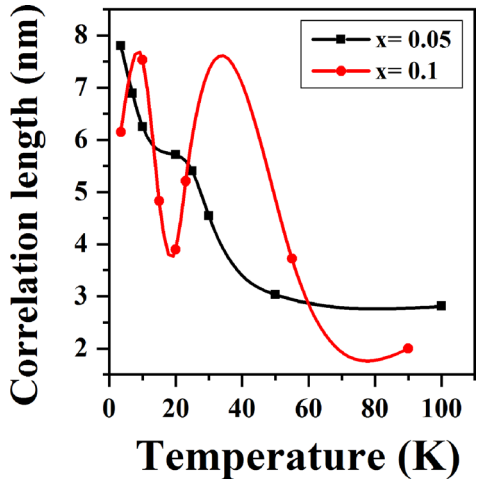

FIG. 11. Temperature dependence of correlation length of the spiral component for x = 0.05 and x = 0.1.

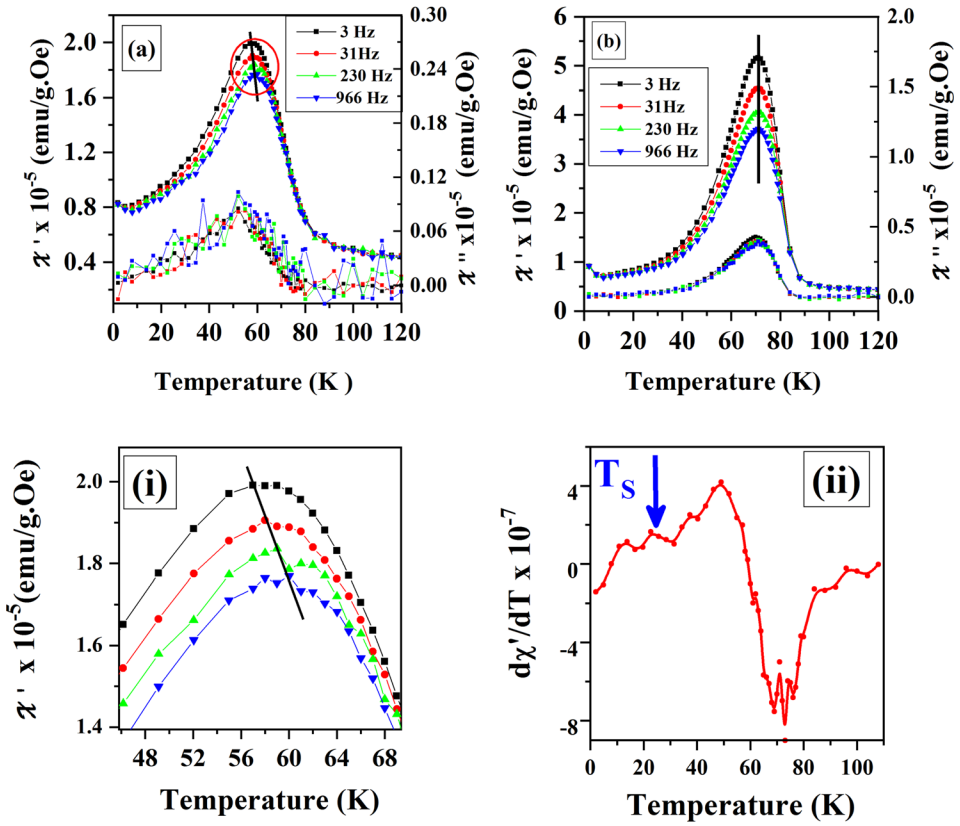

FIG. 12. Real and imaginary parts of ac susceptibility versus temperature at different frequencies: 3, 31, 230 and 966 Hz for $Zn_xCo_{1-x}Cr_2O_4$, (a) $x = 0.05$ and (b) $x = 0.1$, respectively. (i) depicts the expanded view of the peak shift with frequency for $x = 0.05$. (ii) depicts $\frac{d\chi'}{dT}$ versus temperature at 966 Hz for $x = 0.05$.

magnetization (M) with magnetic field (H) at 2 K is shown in Fig. 14(a). The magnetization does not saturate up to 140 kOe irrespective of measuring temperatures. The magnetization increases readily up to 20 kOe and then linearly increases up to 140 kOe. The non-saturation of magnetization results from the large contribution of disordered spins at the surface. Figure 14(b) depicts the change in maximum magnetization measured at 140 kOe with varying temperature for both samples. One may note that the magnetization measured at maximum applied field decreases with increase in temperature in both samples as expected. However, the difference in magnetization is uniformly maintained throughout the temperature range. Figure 14(b) depicts the temperature dependent coercivity for $x = 0.05$ and 0.1. With increase in Zn concentration from 0.05 to 0.1, the coercivity increases from 3.2 kOe to 5.2 kOe. The observed coercivity is found to be two orders magnitude higher than that of bulk $CoCr_2O_4$ at 2 K. Franco and e Silva[29] have reported that Zn incorporation in $CoFe_2O_4$ spinel compounds results in decrease in saturation magnetization and coercivity. The decreasing trend is an indication of Co^{2+} being replaced by Zn^{2+} ions in $Co_{1-x}Zn_xFe_2O_4$ mixed ferrite. However, although in the present case we have incorporated Zn ions in a similar spinel structure $CoCr_2O_4$, one may notice that, while the maximum magnetization decreases from 9 to 8 emu/g, the coercivity increases by 2 kOe at 2 K with an increase in the non-magnetic Zn ion concentration from 0.05 to 0.1. This clearly indicates that B site ions play a significant role in producing such unusual behavior. We have further explained such behavior by considering different models like Neel's two sub-lattice model and the Yafet-Kittel model used generally in ferrimagnetic materials.

According to the Neel's two sub-lattice model, the magnetic moments of ions on the A and B sub-lattices are aligned anti-parallel to each other and their spins have a collinear structure as shown in Fig. 15(a). While increase in non-magnetic Zn^{2+} ions which occupy A-site results in decrease in the magnetic moment of A-site, the magnetic moment of B-site (Cr^{3+}) remains constant. The theoretical magnetic moment, $\mathbf{n_B}^{\mathbf{th}} = \mathbf{M_B} - \mathbf{M_A}$, has been calculated as

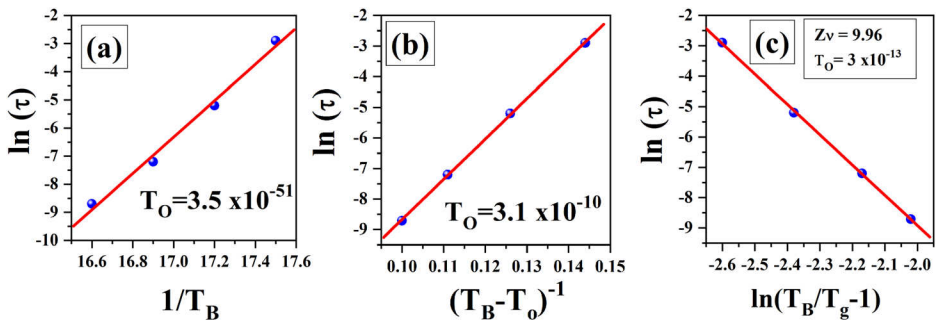

FIG. 13. (a) The relaxation time (τ) is fitted using Neel-Arrhenius law for $Zn_{0.05}Co_{0.95}Cr_2O_4$. (b) and (c) depict fitting using and Vogel-Fulcher's law and power law, respectively.

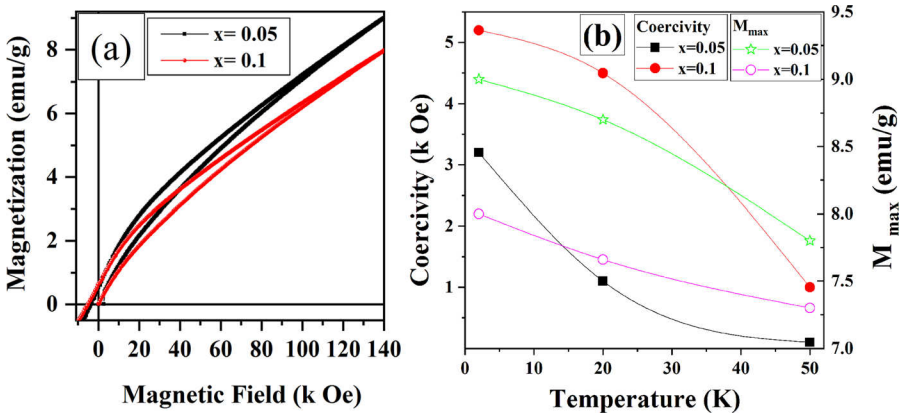

FIG. 14. (a) Magnetic field (H) dependent magnetization at 2 K. (b) temperature dependent coercivity and maximum magnetization of $Zn_xCo_{1-x}Cr_2O_4$(x = 0.05, 0.1).

3.15 μ_B for x = 0.05 and 3.3 μ_B for x = 0.1. The experimental magnetic moment, $\mathbf{n_B}^{\mathbf{exp}}$, is found to be one order magnitude less than the theoretical one. The reduction in magnetization could be due to the existence of random canting of spins at the surfaces due to nanometer size of the particles.[30] The decrease in the magnetic moment with increase in Zn concentration indicates a possibility of a non-collinear spin structure which can be explained on the basis of three sub-lattice model suggested by the Yafet-Kittel (Y-K) model.[31] According to Y-K model, the B lattice is divided into two sub-lattices, i.e., B_1 and B_2. Each sub-lattice is having magnetic moments equal and each one is oppositely canted at the same angle, α_{YK} as shown in Fig. 15(b). The net magnetic moment is given by $n_B{}^{exp} = M_B \cos\alpha_{YK} - M_A$, where $n_B{}^{exp}$ is expressed in Bohr magneton. The Y-K angle (α_{YK}) is expressed as

$$\alpha_{Y-K} = \mathrm{Cos}^{-1}\left(\frac{n_B^{exp} + M_A}{M_B}\right).$$

The non-zero Y-K angle (α_{YK}) suggests that the magnetization behavior cannot be explained on the basis of Neel two sub-lattice model due to the presence of the non-collinear spin structure at the B site, which strengthens the B-B interaction at the cost of A-B interaction.[32] The collinear spin structure results in zero Y-K angles. We have

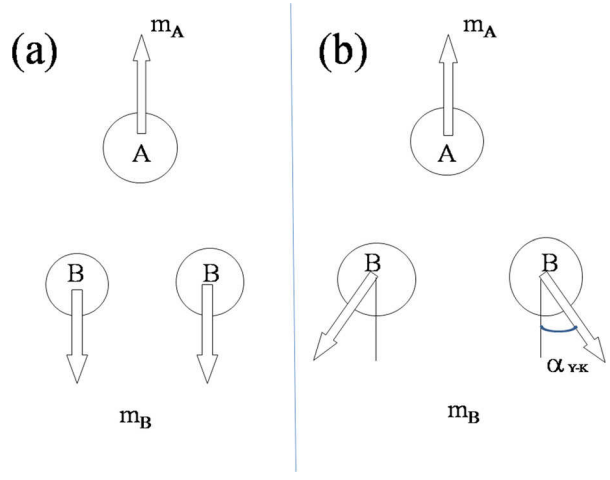

FIG. 15. Schematic representation of spin orientation at A and B sites for (a) collinear (Neel's model) and (b) non-collinear (Y-K) model.

estimated the Y-K angles using the above equation and they are found to be 57.5° and 59.7° for x = 0.05 and 0.1, respectively. The non-zero Y-K angle thus confirms the non-collinear spin structure and favors the triangular spin arrangement in the B site. The increase in the Y-K angle with increase in Zn concentration could be the origin of increase in coercivity with increasing Zn concentration. The increase in the Y-K angle with increase in Zn concentration also supports the decrease in T_C observed from dc χ vs. T measurement.

In order to calculate the effective magnetic moment (μ_{eff}), the high temperature susceptibility data in the paramagnetic region is used to fit the Curie-Weiss equation $\chi = \frac{C}{(T-\theta_{CW})}$, where C is the Curie constant and (θ_{CW}) is the Curie-Weiss temperature. The effective magnetic moment is calculated using the relation $\mu_{eff} = (3CK_B/N)^{1/2}$, where C is the slope obtained from the inverse susceptibility versus temperature. The fitting parameters are shown in Table II.

The calculated values of μ_{eff} are 6.68 μ_B and 7.42 μ_B for x = 0.05 and 0.1, respectively. As Zn content increases, magnetic moments decrease in the sub-lattice A and increases in the sub-lattice B. Hence, the μ_{eff} increases with Zn concentration. Further it is observed that, at 2 K, the maximum magnetic moment per atom ($\mathbf{n_B}^{\mathbf{exp}}$) in the direction of field is found to be an order of magnitude less than the magnetic moment obtained from the paramagnetic range (μ_{eff}). The large paramagnetic moment is also evidenced from the non-saturation behavior of magnetization at 140 kOe field which could be due to magnetic correlation in the paramagnetic regime.[10] The orbital quenched (spin-only) moment is calculated using the relation ($\mu_S = 2(S(S+1))^{1/2}$) for free ions Co^{2+} and Cr^{3+} (S = 3/2) and is noted as 3.88 μ_B. For x = 0.05, the total quenched moment is calculated using $((1 - x)\mu_{Co}{}^2 + 2\ \mu_{Cr}{}^2)^{1/2}$. The obtained value of quenched moment (6.7 μ_B) is close to effective magnetic moment for x = 0.05. In order to explain the higher μ_{eff} observed for x = 0.1, the unquenched orbital contribution from Co^{2+} is considered and is calculated using the relation $\mu_{L+S} = [(4S(S+1) + L(L+1)]^{1/2}$. The unquenched moment obtained (7.37 μ_B) is close to μ_{eff} for x = 0.1 (7.42 μ_B). In the case of x = 0.05, the measured μ_{eff} is close to quenched moment (6.7μ_B). While this may be unexpected for Co^{2+} in a tetrahedral coordination having no orbital degeneracy, the presence of low lying e^g, t^{2g} excited state could be a source

TABLE II. Results from fitting the inverse magnetic susceptibility data to the Curie-Weiss equation to the high temperature inverse susceptibility data for $Zn_xCo_{1-x}Cr_2O_4$ ($x = 0.05, 0.1$). Θ_{cw} is taken as the x-intercept of the inverse susceptibility. f is defined as the absolute ration of Θ_{cw} to T_C.

Sample	Quenched (spin-only) μ_{eff} (μ_B)	Unquenched (spin + orbital) μ_{eff} (μ_B)	Measured $\mu_{eff} = (3CK_B/N)^{1/2}$ (μ_B)	Θcw (K)	Curie constant (C)	T_c (K)	$f = \lvert\Theta_{cw}\rvert/T_c$
X = 0.05	6.7	7.46	6.68	−445	5.6	90	4.9
X = 0.1	6.6	7.37	7.42	−360	6.9	87.4	4.1

for the increased moment.[33] The frustration index, f, is defined as the absolute ratio of $|\Theta_{cw}|/T_C$ and is calculated as 4.9 and 4.1 for $x = 0.05$ and 0.1, respectively.

IV. CONCLUSIONS

Pure $Zn_xCo_{1-x}Cr_2O_4$ ($x = 0.05, 0.1$) nanoparticles of size 10 nm were synthesized through the conventional co-precipitation technique followed by calcination at 500 °C. XRD patterns confirmed the cubic spinel structure without any impurity phase. Lattice parameter decreased with increase in Zn concentration, due to the less ionic nature of Zn than Co, and/or due to decrease in A-B repulsion. Cation distribution of $Zn_xCo_{1-x}Cr_2O_4$ studied through EXAFS confirmed that while Cr^{3+} ions preferred B site, Zn^{2+} and Co^{2+} ions occupied the A site. From dc magnetization and diffuse neutron scattering, with increase in x from 0.05 to 0.1, we revealed that the paramagnetic to ferrimagnetic transition, T_C, decreased from 90 K to 87.4 K, T_S from 26 K to 24 K, and the spin lock-in transition, T_L, observed at 10 K remained unchanged. Temperature dependent ac magnetic susceptibility measurement showed the dispersion behavior with frequency for $x = 0.05$ which was found to be absent in $x = 0.1$. The phenomenological models like Vogel-Fulcher and power law were fitted and the coexistence of spin-glass and cluster glass in $x = 0.05$ was confirmed. Neel's two sub-lattice model failed to explain the decrease in saturation magnetization with increase in Zn concentration measured from the hysteresis loop at 2 K. This was well explained by considering the three sub-lattice models suggested by Yafet-Kittel (Y-K). The increase in Y-K angles with increase in Zn concentration further indicated the triangular spin arrangement in the B site resulting in decreasing of A-B exchange interaction, hence decrease in T_C.

ACKNOWLEDGMENTS

C.R. acknowledges UGC-DAE CSR, Indore, India, for funding the project (CSR-IC/BL-29/CRS-126) to carry out EXAFS measurements. The authors acknowledge Dr. S. N. Jha, RRCAT, Dr. D. Bhattacharya, BARC, and Dr. D. M. Phase, UGC-DAE CSR, Indore, for their help during EXAFS measurements in beam line BL-9 of Indus-2. Beam line BL-9 of Indus-2, RRCAT is acknowledged for EXAFS measurements. The authors also acknowledge Heinz Maier-Leibnitz Zentrum (MLZ) center at Garching, Germany, for providing beam time to carry out the diffused Neutron Scattering Experiment.

[1]B. D. Cullity, *Introduction to Magentic Materials* (Addison-Wesley Publishing Company, Inc., 1972).
[2]Y. Yamasaki, S. Miyasaka, Y. Kaneko, J.-P. He, T. Arima, and Y. Tokura, "Magnetic reversal of the ferroelectric polarization in a multiferroic spinel oxide," Phys. Rev. Lett. **96**(20), 207204 (2006).
[3]K. Tomiyasu, J. Fukunaga, and H. Suzuki, "Magnetic short-range order and reentrant-spin-glass-like behavior in $CoCr_2O_4$ and $MnCr_2O_4$ by means of neutron scattering and magnetization measurements," Phys. Rev. B **70**(21), 214434 (2004).
[4]J. K. Galivarapu, D. Kumar, A. Banerjee, V. Sathe, G. Aquilanti, and C. Rath, "Effect of size reduction on cation distribution and magnetic transitions in $CoCr_2O_4$ multiferroic: EXAFS, magnetic and diffused neutron scattering measurements," RSC Adv. **6**(68), 63809–63819 (2016).
[5]C. Rath, P. Mohanty, and A. Banerjee, "Magnetic properties of nanoparticles of cobalt chromite," J. Magn. Magn. Mater. **323**(12), 1698–1702 (2011).
[6]K. Severance, R. Edge, and W. E. Sharp, "Spin glass behavior in a single crystal of chromite," Am. Miner. **78**, 724–732 (1993).
[7]D. Das, R. Biswas, and S. Ghosh, "Systematic analysis of structural and magnetic properties of spinel CoB_2O_4 (B = Cr, Mn and Fe) compounds from their electronic structures," J. Phys.: Condens. Matter **28**(44), 446001 (2016).
[8]A. Aqeel, N. Vlietstra, J. A. Heuver, G. E. W. Bauer, B. Noheda, B. J. van Wees, and T. T. M. Palstra, "Spin-Hall magnetoresistance and spin Seebeck effect in spin-spiral and paramagnetic phases of multferroic $CoCr_2O_4$ films," Phys. Rev. B **92**, 224410 (2015).
[9]D. Kumar, A. Banerjee, A. Mahmoud, and C. Rath, "Cation distribution dependent magnetic properties in $CoCr_{2-x}Fe_xO_4$($x = 0.1$ to 0.5): EXAFS, Mössbauer and magnetic measurements," Dalton Trans. **46**(31), 10300–10314 (2017).
[10]M. C. Kemei, S. L. Moffitt, D. P. Shoemaker, and R. Seshadri, "Evolution of magnetic properties in the normal spinel solid solution $Mg_{1-x}Cu_xCr_2O_4$," J. Phys.: Condens. Matter **24**(4), 046003 (2012).
[11]M. C. Kemei, S. L. Moffitt, L. E. Darago, R. Seshadri, M. R. Suchomel, D. P. Shoemaker, K. Page, and J. Siewenie, "Structural ground states of (A, A′) Cr_2O_4 (A= Mg, Zn; A′= Co, Cu) spinel solid solutions: Spin-Jahn-Teller and Jahn-Teller effects," Phys. Rev. B **89**(17), 174410 (2014).
[12]See http://www.rrcat.gov.in/technology/accel/srul/beamlines/index.html for beam line specifications.
[13]S. Basu, C. Nayak, A. Yadav, A. Agrawal, A. Poswal, D. Bhattacharyya, S. Jha, and N. Sahoo, "A comprehensive facility for EXAFS measurements at the INDUS-2 synchrotron source at RRCAT, Indore, India," J. Phys.: Conf. Ser. **493**, 012032 (2014).
[14]M. Newville, B. Ravel, D. Haskel, J. Rehr, E. Stern, and Y. Yacoby, "Analysis of multiple-scattering XAFS data using theoretical standards," Physica B **208**, 154–156 (1995).
[15]Y. Okamoto, H. Nakano, T. Imanaka, and S. Teranishi, "X-ray photoelectron spectroscopic studies of catalysts—Supported cobalt catalysts—," Bull. Chem. Soc. Jpn. **48**(4), 1163–1168 (1975).
[16]B. C. Melot, J. E. Drewes, R. Seshadri, E. M. Stoudenmire, and A. P. Ramirez, "Magnetic phase evolution in the spinel compounds $Zn_{1-x}Co_xCr_2O_4$," J. Phys.: Condens. Matter **21**, 216007 (2009).
[17]F. De Groot, "High-resolution X-ray emission and X-ray absorption spectroscopy," Chem. Rev. **101**(6), 1779–1808 (2001).
[18]L. Grunes, "Study of the K edges of 3 d transition metals in pure and oxide form by x-ray-absorption spectroscopy," Phys. Rev. B **27**(4), 2111 (1983).
[19]G. Aquilanti, A. Cognigni, and M. Anis-ur-Rehman, "Cation distribution in Zn doped cobalt nanoferrites determined by X-ray absorption spectroscopy," J. Supercond. Novel Magn. **24**(1-2), 659–663 (2011).
[20]R. Plumier, "Reinvestigation of magnetic structures of $CoCr_2O_4$ and $MnCr_2O_4$ obtained by neutron diffraction," J. Appl. Phys. **39**(2), 635–636 (1968).
[21]G. Lawes, B. Melot, K. Page, C. Ederer, M. A. Hayward, T. Proffen, and R. Seshadri, "Dielectric anomalies and spiral magnetic order in $CoCr_2O_4$," Phys. Rev. B **74**, 024413 (2006).

[22]I. Golosovsky, I. Mirebeau, G. André, D. Kurdyukov, Y. A. Kumzerov, and S. Vakhrushev, "Magnetic ordering and phase transition in MnO embedded in a porous glass," Phys. Rev. Lett. **86**(25), 5783 (2001).
[23]K. Dwight and N. Menyuk, "Distant-neighbor B-B interactions in cobalt chromite," J. Appl. Phys. **40**(3), 1156–1157 (1969).
[24]K. Binder and A. P. Young, "Spin glasses: Experimental facts, theoretical concepts, and open questions," Rev. Mod. Phys. **58**(4), 801 (1986).
[25]J. A. Mydosh, *Spin Glasses: An Experimental Introduction* (Taylor and Francis, 1993).
[26]F. B. Calleja and S. Fakirov, *Microhardness of Polymers* (Cambridge University Press, 2007).
[27]J. L. Tholence, *Magnetic Susceptibility of Superconductors and Other Spin Systems*, edited by R. A. Hein, T. L. Francavilla, and D. H. Liebenberg (Plenum Press, NewYork, 1991), p. 503.
[28]P. Poddar, T. Telem-Shafir, T. Fried, and G. Markovich, "Dipolar interactions in two-and three-dimensional magnetic nanoparticle arrays," Phys. Rev. B **66**(6), 060403 (2002).
[29]A. Franco, Jr. and F. e Silva, "Effect of the Zn content in the magnetic properties of $Co_{1-x}Zn_xFe_2O_4$ mixed ferrites," J. Appl. Phys. **113**(17), 17B513 (2013).
[30]J. M. D. Coey, "Noncollinear spin arrangement in ultrafine ferrimagnetic crystallites," Phys. Rev. Lett. **27**(17), 1140 (1971).
[31]Y. Yafet and C. Kittel, "Antiferromagnetic arrangements in ferrites," Phys. Rev. **87**(2), 290 (1952).
[32]S. S. Jadhav, S. E. Shirsath, S. M. Patange, and K. Jadhav, "Effect of Zn substitution on magnetic properties of nanocrystalline cobalt ferrite," J. Appl. Phys. **108**(9), 093920 (2010).
[33]J. D. Lee, *Concise Inorganic Chemistry* (John Wiley & Sons, 2008).